The Role of the Unsteady Surface Wave-Driven Ekman–Stokes Flow in the Accumulation of Floating Marine Litter

Cunningham, H. J.; Higgins, C.; van den Bremer, T. S.

Important note
To cite this publication, please use the final published version (if applicable).
Please check the document version above.

JGR Oceans

Correspondence to:
H. J. Cunningham,
harry.cunningham.21@ucl.ac.uk

Author Contributions:
Conceptualization: C. Higgins, T. S. van den Bremer
Investigation: C. Higgins, T. S. van den Bremer
Methodology: C. Higgins, T. S. van den Bremer
Supervision: C. Higgins, T. S. van den Bremer
Writing – review & editing: C. Higgins, T. S. van den Bremer

The Role of the Unsteady Surface Wave-Driven Ekman–Stokes Flow in the Accumulation of Floating Marine Litter

H. J. Cunningham[1,2] , C. Higgins[1], and T. S. van den Bremer[1,3]

[1]Department of Engineering Science, University of Oxford, Oxford, UK, [2]Centre for Artificial Intelligence, University College London, London, UK, [3]Faculty of Civil Engineering and Geosciences, Delft University of Technology, Delft, The Netherlands

Abstract Recently, a number of authors have used global particle tracking simulations to identify the effect that different surface currents have on marine litter accumulation, including the role of surface waves through the Stokes drift. However, in the upper-ocean boundary layer and in the presence of the Coriolis force, a wave-driven Eulerian flow forms that must be superimposed onto the Stokes drift in order to obtain the correct Lagrangian velocity. Taking into account both the Coriolis–Stokes force and the surface wave stress, Higgins et al. (2020), https://doi.org/10.1029/2020GL089189 derived an expression for this unsteady wave-driven Eulerian-mean flow in the form of a convolution between the Stokes drift and the so-called Ekman–Stokes kernel. In this paper, we apply this Ekman–Stokes kernel to generate a 12-year global hindcast of the wave-driven Eulerian current and show that its inclusion in particle tracking simulations has a significant effect on the distribution of small floating marine litter, such as microplastics. Using Lagrangian simulations, we find that the wave-driven Eulerian current is sensitive to the value of viscosity but generally opposes the dispersive behavior of the Stokes drift, reducing the amount of cross-Equator particle transport and transport to the polar regions, resulting in closer agreement between modeled and observed microplastic distributions.

Plain Language Summary Though marine litter is found to accumulate near the surface in each of the subtropical ocean gyres, its transport pathways and accumulation behaviors are poorly understood. Particle tracking simulations have been used to model the distribution of marine litter. In recent studies, the effects of wave-driven transport have been considered by simply superimposing the Stokes drift (net drift induced by surface waves) onto other non-wave-driven surface currents. However, due to the Earth's rotation and turbulent behavior in the upper-ocean boundary layer, the Stokes drift also generates an additional wave-driven Eulerian-mean flow, known as the Ekman–Stokes flow. This wave-driven Eulerian flow must be superimposed on the Stokes drift to form the correct wave-driven Lagrangian current. Using the convolution expression derived by Higgins et al. (2020), https://doi.org/10.1029/2020GL089189, we develop a 12-year global hindcast for the unsteady wave-driven Eulerian current and subsequently perform Lagrangian particle tracking simulations to model the accumulation of small floating marine litter, such as microplastics. We find that the wave-driven Eulerian current has a significant effect on microplastic pathways, reducing cross-Equator transport and transport to the polar regions, increasing the retention of particles in the subtropical ocean gyres and causing closer agreement between modeled and observed microplastic distributions.

1. Introduction

Plastic litter is considered ubiquitous in the marine environment, having been found in all of the world's ocean basins, in the polar regions and at the Equator (van Sebille et al., 2015). Presently, there is a lack of knowledge regarding the transportation and distribution of this floating marine litter (van Sebille et al., 2020). Very few reliable and comparable data-sets exist on floating marine litter concentrations in the open ocean (Stanev & Ricker, 2019), and such studies are themselves very costly and prone to biases (Hardesty et al., 2017). As a result, numerical modeling has been used to advance our understanding of marine litter transport and accumulation patterns (e.g., Onink et al. (2019)).

It has been shown using both observational data and particle tracking simulations that buoyant microplastics accumulate at the center of each subtropical ocean gyres in each of the five major ocean basins (Cózar et al., 2014; Eriksen et al., 2014; Law et al., 2014; van Sebille et al., 2015). The location of these accumulation zones, often termed 'ocean garbage patches', is attributed to the convergence of large scale open-ocean surface currents,

which efficiently transport floating microplastics over large distances (Kubota, 1994; Kubota et al., 2005; Onink et al., 2019). Indeed, Ekman currents in the upper ocean driven by surface winds and the action of the Earth's rotation, create regions of convergence in all five subtropical ocean gyres, and have been shown to be accurately predict the large-scale distribution of floating microplastics (Kubota, 1994; Martinez et al., 2009; Onink et al., 2019; van Sebille et al., 2020).

However, surface ocean circulation is composed of several current components, including Ekman currents, geostrophic currents, and wave-induced Stokes drift. Importantly, previous studies on the accumulation dynamics of floating microplastics which include the effects of wave-induced transport have simply superimposed the Stokes drift on the Eulerian current flow fields. Such studies have shown that the Stokes drift does not contribute to microplastic accumulation in the subtropics but leads to increased transport to the polar regions (Onink et al., 2019), changes the entrainment of particles from east to west in the Indian Ocean (Dobler et al., 2019), and causes seasonal variation in the transportation of different sized particles in the sea of Japan (Iwasaki et al., 2017).

However, the Stokes drift and Eulerian currents do not evolve independently, and the presence of surface gravity waves modifies the Eulerian flow field through the Stokes forces (Craik & Leibovich, 1976; Suzuki & Fox-Kemper, 2016). On a rotating Earth, the Coriolis force associated with the Stokes drift generates an Eulerian-mean flow in the turbulent upper-ocean boundary layer (Lewis & Belcher, 2004; Polton et al., 2005; Xu & Bowen, 1994). This wave-driven Eulerian current must be added to the Stokes drift to obtain the correct wave-induced Lagrangian velocity relevant to the transportation of marine litter.

Wave-driven Eulerian currents have been explored in detail in the literature. Ursell (1950) showed that in a rotating, inviscid ocean, the Lagrangian-mean velocity induced by a periodic wave train must be zero in an average over several inertial periods. Hasselmann (1970) verified this result by showing that planetary vorticity results in a so-called Coriolis Stokes forcing, $f \times u_S$, in the Eulerian-mean equations. This drives an 'anti-Stokes' Eulerian flow which cancels the Stokes drift in inertial mean, resulting in no net Lagrangian-mean mass transport. In contrast to the inviscid and rotating reference frame assumptions made by Hasselmann (1970), and Longuet-Higgins (1953) considered a non-rotating but viscid approach. For any nonzero viscosity a thin viscous boundary layer forms near the surface, causing an increase in the mass-transport (Lagrangian) velocity at the surface as vorticity is transported into the interior of the fluid. This results in a wave stress on the flow at the base of the viscous boundary layer, so that the gradient of the Lagrangian velocity there is twice the corresponding value for irrotational flow (Longuet-Higgins, 1953). Hence, the wave-induced Lagrangian flow is notably modified by two different approaches: Hasselmann's inviscid but rotating approach and Longuet-Higgins' viscid but non-rotating approach.

Recently, Higgins et al. (2020) derived the unsteady Ekman–Stokes Eulerian response to a time-varying Stokes drift, considering both the Coriolis–Stokes forcing (Hasselmann, 1970) and surface wave stress boundary condition (Longuet-Higgins, 1953) for the case of a constant eddy viscosity and quasi-monochromatic wavefield. Described by a convolution between the unsteady Stokes drift and an Ekman–Stokes kernel function, Higgins et al. (2020) showed that the unsteady wave-driven Eulerian current has a significant impact on near-surface flow, altering the predictions of microplastic trajectories. The kernel convolution provides a less computationally expensive treatment of the Coriolis–Stokes forcing than that of fully coupled ocean general circulation models (OGCMs), which require simultaneous solution of a wave and ocean transport model. Unlike OGCMs, the kernel convolution allows the use of ocean surface current hindcast datasets to easily create a global flow field through superposition of individual current components.

In this paper, we examine the effect of the wave-driven Ekman–Stokes Eulerian current on the trajectories of floating marine litter, in particular microplastics, by performing particle tracking simulations. Unlike Ekman currents and the Stokes drift, no observational datasets exist for the wave-driven Eulerian current. Hence, we develop global datasets by applying the Higgins et al. (2020) wave-driven Eulerian flow model for two different viscosity models to wavefield data from WaveWatch III (Tolman, 2009) and Globcurrent. We show that the wave-driven Eulerian current has a significant effect on the location of accumulation zones and the transport mechanisms of floating microplastics.

This paper is laid out as follows: Section 2 will describe the methods and data used to generate the wave-driven Ekman–Stokes Eulerian current and perform the Lagrangian particle tracking simulations. Section 3 will examine the results of both the wave-driven Eulerian current datasets and the particle tracking simulations, also comparing

to observed distributions, and the final results and conclusions are discussed in Section 4. We examine possible extensions to our model and avenues for future work in Section 5.

2. Methods and Data

In the following subsections, we describe how we generated the wave-driven Eulerian current datasets and the configuration of the particle tracking simulations using Ocean Parcels (Delandmeter & Van Sebille, 2019). Section 2.1 briefly reviews the derivation of the Ekman–Stokes kernel. Section 2.2 describes the datasets used in the implementation of the kernel function in Section 2.3, which also considers how best to accurately reflect the sea state when defining the wave parameters. Lastly, Section 2.4 describes the methods used to perform particle tracking simulations using Ocean Parcels.

2.1. Unsteady Wave-Driven Ekman–Stokes Eulerian Current

The wave-driven Ekman–Stokes model derived by Higgins et al. (2020) considers both the Coriolis–Stokes forcing and the surface wave stress boundary condition. The wave stress condition arises due to the formation of a thin viscous boundary layer near the surface (cf. Seshasayanan & Gallet, 2019). Through both the Coriolis–Stokes forcing and the wave stress, the Stokes drift acts as a forcing which generates the Ekman–Stokes Eulerian-mean flow in conjunction with the action of the Earth's rotation and the turbulent shear in the ocean's surface layer.

Taking the momentum equations for the wave-induced flow to second-order in wave steepness and wave-averaging gives the equations for the Eulerian-mean flow,

$$\partial_t \boldsymbol{u} + \boldsymbol{f} \times (\boldsymbol{u} + \boldsymbol{u}_s) = -\nabla p + \nu \nabla^2 \boldsymbol{u}, \qquad \nabla \cdot \boldsymbol{u} = 0, \tag{1}$$

where $\boldsymbol{f} = f\hat{\boldsymbol{z}}$ is the (traditional) Coriolis vector, p the pressure, ν the turbulent eddy viscosity (taken to be a constant), $\boldsymbol{u}_S$ the Stokes drift and $\boldsymbol{u}$ the Eulerian mean flow velocity. Assuming that the horizontal pressure gradients and horizontal variation of the wavefield are negligible to leading order, given the rapid variation of the flow in the vertical compared with the horizontal, Equation 1b yields that the vertical velocity component w is also negligible, which in turn implies that $\nabla p = 0$. Introducing complex notation $\mathcal{U} = u + iv$ and $\mathcal{U}_S = u_s + iv_s$, we obtain the Ekman–Stokes equations (cf. Higgins et al., 2020),

$$\partial_t \mathcal{U} + if(\mathcal{U} + \mathcal{U}_S) = \nu \partial_z^2 \mathcal{U}, \qquad \partial_z \mathcal{U} = \partial_z \mathcal{U}_S|_{z=0}, \qquad \lim_{z \to -\infty} \mathcal{U} = 0. \tag{2}$$

Consequently, the fluid velocities are driven by the wavefield in two ways: first, by the Coriolis–Stokes forcing in the fluid interior and second, by the virtual wave stress at the surface.

In a realistic wavefield, the wave amplitude changes on a timescale shorter than or similar to that with which transients decay. We therefore consider the time-dependent solution to the Ekman–Stokes equations in order to capture the unsteadiness of the wave-driven Eulerian response to the temporally varying Stokes drift. By solving Equation 2 using a Laplace transform in time and applying the Laplace Convolution Theorem, the Ekman–Stokes flow is described as a convolution between the forcing Stokes drift, $\mathcal{U}_S$, and the Ekman–Stokes kernel function, K.

$$\mathcal{U}(\boldsymbol{x}, z, t) = \mathcal{U}_S(\boldsymbol{x}, t) *_{(t)} K(t, z; f, \nu), \tag{3}$$

$$K(t, z; f, \nu) = 2k\sqrt{\nu}e^{-ift}\frac{e^{-z^2/(4\nu t)}}{\sqrt{\pi t}} - ife^{ift}\frac{e^{-z^2/(4\nu t)}}{2}\sum_{\pm}\mathrm{erfcx}\left(\sqrt{4k^2\nu t} \pm \frac{z}{\sqrt{4\nu t}}\right), \tag{4}$$

where f is the Coriolis parameter, ν the eddy viscosity and k the wavenumber. The summation $\sum_{\pm}$ denotes the sum of the plus and minus terms. The kernel is written in terms of the scaled complementary error function $\mathrm{erfcx}(x) = e^{x^2}(1 - \mathrm{erf}(x))$ for the sake of neatness and to avoid numerical overflow when implementing the convolution. It is worth noting that, although slowly time-varying in reality, both the wavenumber and viscosity are considered to be constants in the mathematics. At the surface, where $z = 0$, the kernel simplifies to:

$$K(t; f, \nu) = 2k\sqrt{\nu}e^{-ift}\frac{1}{\sqrt{\pi t}} - ife^{-ift}\mathrm{erfcx}\left(\sqrt{4k^2\nu t}\right). \tag{5}$$

Table 1
Overview of the Data Sets Used for the to Calculate the Wave-Driven Eulerian Current and to Perform the Lagrangian Particle Simulation

Variable	Data set	Spatial resolution	Temporal resolution	Source
Geostrophic currents	GlobCurrent v3 Geostrophic Currents	0.25°	24 hr	Rio et al. (2014)
Ekman currents	GlobCurrent v3 Ekman Hs Currents	0.25°	3 hr	Rio et al. (2014)
Total currents	GlobCurrent v3 Total Hs Currents	0.25°	3 hr	Rio et al. (2014)
Stokes drift	WaveWatch III Surface Stokes Drift	0.5°	3 hr	Ardhuin et al. (2009)
Peak frequency	WaveWatch III f_p	0.5°	3 hr	Tolman, (2009)
Significant wave height	WaveWatch III H_s	0.5°	3 hr	Tolman, (2009)
Surface wind stress	NOAA blended surface wind stress	0.25°	6 hr	Zhang et al. (2006)

Taking the limit as $\nu \to 0^+$, we recover the Hasselmann (1970) solution, in which the wave-driven Eulerian current opposes the Stokes drift that caused it and induces undamped inertial oscillations,

$$K(t; f) = -if \exp(-ift).$$ (6)

Taking the limit $f \to 0^+$ removes any Coriolis–Stokes forcing, representative of conditions at the Equator, and we recover the Longuet-Higgins (1953) solution for boundary layer streaming,

$$K(t; \nu) = \frac{2k\sqrt{\nu}}{\sqrt{\pi t}}.$$ (7)

The behavior of the kernel is therefore seen to operate on two different timescales: an inertial timescale $\tau = ft$, and a wave-associated viscous timescale $T = 4k^2\nu t$.

2.2. Ocean Surface Current Data Sets

In order to model the different surface current components and to generate the wave-driven Eulerian current hindcast, we used several reanalysis surface current datasets. For the Ekman and geostrophic currents, we used datasets available from the GlobCurrent project which makes use of satellite observations and in situ drifter measurements to obtain estimates for surface currents (Rio et al., 2014). For the surface Stokes drift we used the reanalysis data set from the IOWAGA project (Rascle & Ardhuin, 2013), derived from the WaveWatch III hindcast data set (Tolman, 2009) which is forced using winds from the Climate Forecast System Reanalysis (CFSR) project (Saha et al., 2010). Much of the reanalyses focused on validating the wind forcing using altimeter and buoy data, providing significant improvement in the estimations for the surface Stokes drift, which is globally larger than previously estimated (Saha et al., 2010). The total currents data set represents the addition of the geostrophic and Ekman currents and is an available GlobCurrent product.

It must be noted that the GlobCurrent and WaveWatch III datasets are not truly independent. When measuring the Ekman currents, the signal is filtered to remove other ageostrophic noise such as tides and the Stokes drift. However, this filtering is not perfect, and the summation of both datasets leads to an overestimation of the Stokes drift, as noted by Onink et al. (2019).

A summary of the datasets used in this project is available in Table 1, which also includes the peak wave frequency data set from WaveWatch III used to calculate the wavenumber k using the deep-water linear dispersion

relationship, and the NOAA blended surface wave stress (Zhang et al., 2006) for use in the Mellor–Yamada 2.5 level turbulence closure model. It is noted that the surface wave stress data set is not available from 2012 onwards, therefore data from 2011 is reused for the final years of the data generation process.

2.3. Implementation of the Convolution Kernel

Implementing the convolution requires several assumptions about the flow field and the data we are provided with. First, the kernel $K(t; f, \nu)$ Equation 5 is derived assuming continuous time. Since the data values are recorded at 3-hourly intervals, we assume a constant value of the Stokes drift between sampling times. The convolution at the nth time point can then be expressed as a summation over $k < n$ time intervals δt, where over each interval the kernel is evaluated at $(k + 1)\delta t$. It is also assumed that the initial condition is $\mathcal{U}|_{t=0} = 0$, as for the long time series considered the influence of the initial condition decays away. Rewriting the convolution Equation 3 first as an integral and then as a summation of terms, the wave-driven Eulerian velocity at the nth time point $\mathcal{U}_n$ is given by

$$\mathcal{U}_n(\tau_n) = \mathcal{U}_S(\tau_n) *_{(\tau)} K(\tau_n, D) = \int_0^{\tau_n} \mathcal{U}_S(t') K(\tau_n - t') dt' = \sum_{k=0}^{n-1} \mathcal{U}_S(k\delta t) K((n-k)\delta t) \delta t. \tag{8}$$

Computationally, the summation can be expressed as a vector dot product between the forcing Stokes drift and the kernel terms, where the vector of Stokes drift terms is written in descending order of time. This is equivalent to finding the trace of the matrix

$$\mathcal{U}_n = \text{trace}(K \cdot \mathcal{U}_S) \delta t = \text{sum}(\text{diag}(K \cdot \mathcal{U}_S)) \delta t, \tag{9}$$

We implement the convolution at a 3-hr temporal resolution, between 2002 and 2014. The kernel is limited in length for computational efficiency, considering only the last 300 time points at any given n. This is equivalent to 40–50 inertial periods and provides good convergence to solutions that consider a larger time cut-off.

2.3.1. Eddy Viscosity

Setting the value of eddy viscosity is difficult, since it does not represent a unique fluid property but instead reflects the local level of turbulence of the flow. Further, easily accessible eddy viscosity data or representative turbulent coefficients are also hard to come by, and therefore we consider 2 different models of viscosity.

First, we consider the simple case that the viscosity is everywhere and at all times equal to the constant eddy viscosity $\nu = 10^{-2} \text{ m}^2\text{s}^{-1}$ (Huang, 1979). We also consider a correction for the value of eddy viscosity in the equatorial band. In the absence of the Coriolis–Stokes forcing at the Equator where $f = 0$, the wave-driven Eulerian current undergoes boundary layer streaming at the surface. Whilst away from the Equator we have assumed the viscosity to be an eddy viscosity in order to capture the turbulent behavior of the upper ocean mixing layer, without any rotation to drive Ekman dynamics, surface microplastics do not experience the eddy viscosity of the mixed layer and the solution tends to Longuet-Higgins' non-rotating result, for which the value of eddy viscosity is too large. Indeed, the use of an eddy viscosity in the equatorial band causes excessive boundary layer streaming, far greater than the $\times2$ amplification witnessed by Longuet-Higgins. Therefore, the viscosity is linearly reduced between $\pm20°$ latitude from our adopted eddy viscosity to the molecular viscosity of sea water at the Equator, $\nu_{\text{mol}} = 10^{-6} \text{ m}^2\text{s}^{-1}$, as used by Longuet-Higgins in his wave flume calculations.

Second, we use the Mellor–Yamada 2.5 level turbulence model, which assumes that the local level of turbulence can be related to flow properties on the larger, resolved scale. The Mellor–Yamada 2.5 level turbulence model (Mellor & Yamada, 1982) relates ocean diffusivity coefficients for heat and turbulence (K_H and K_q respectively), and turbulent eddy viscosity (A_z), to the turbulent kinetic energy $q^2/2$ and the turbulent length scale l:

$$(A_z, K_H, K_q) = lq(S_M, S_H, S_q), \tag{10}$$

where, for near-surface and near-neutral conditions (Mellor & Blumberg, 2004),

$$(S_M, S_H, S_q) = (0.30, 0.49, 0.20). \tag{11}$$

By assuming the law of the wall for the thin layer of constant stress beneath the sea surface, ignoring the effects of breaking waves,
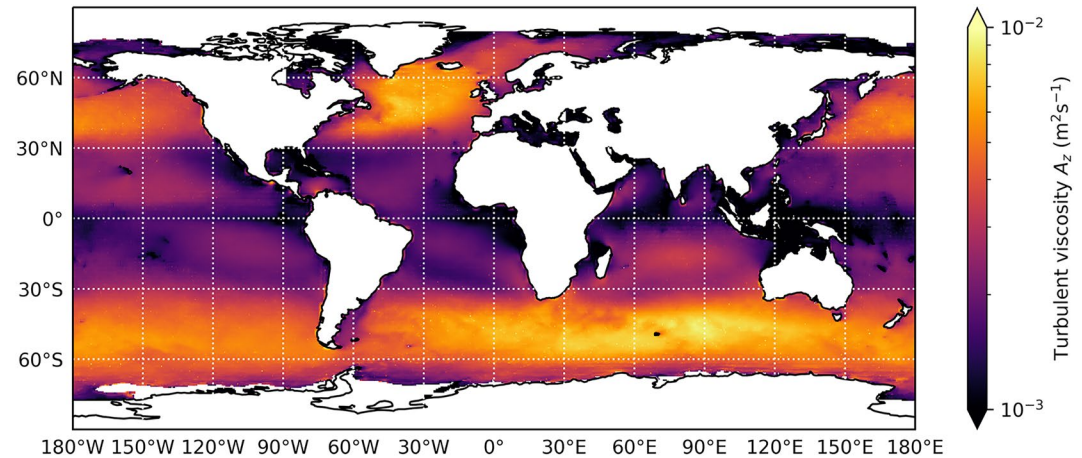
Figure 1. Average turbulent viscosity, A_z, over 2002, calculated using the Mellor–Yamada 2.5 level turbulence model, for $z = 0$.

$$q = u_* = \sqrt{\frac{\tau(0)}{\rho}} \quad \text{and} \quad l = \kappa\,(z + z_0)\,, \tag{12}$$

where u_* is the air-side friction velocity, $\tau(0)$ the surface shear stress, ρ the density of seawater, $\kappa(=0.41)$ the von Karman constant, z the depth below the free surface (distance from the wall) and z_0 the roughness length. Terray et al. (1999) found using measured wave heights and near-surface dissipation data that for $|z| \leq z_0$ ($l \approx \kappa z_0$), $z_0 = 0.85 H_s$ produced a best-fit outcome from the Mellor–Yamada model to the observed data. Using the NOAA blended surface wind stress data set derived from multiple satellite and in-situ measurements (Zhang et al., 2006) and the significant wave height data set from the WaveWatch III hindcast, the global variation of eddy viscosity is in the range $10^{-3} - 10^{-2}$ m^{2}s^{-1}, as shown in Figure 1. Between $\pm 20°$ latitude we again multiply the eddy viscosity by a linearly decreasing function, such that it is equal to its molecular value at the Equator. The advantages of the Mellor–Yamada 2.5 level turbulence model are that we are able to incorporate more realistic spatial and temporal variation of the eddy viscosity into our wave-driven Eulerian current model.

2.3.2. Wavenumber

Like viscosity, the wavenumber is also time-varying due to its dependence on the local instantaneous sea state. Implementing the convolution, we assume both the wavenumber and viscosity to be quasi-stationary in time by averaging over several months. For the Constant viscosity model the wavenumber is averaged over 1,000 time points (125 days) and for the Mellor–Yamada model the wavenumber is averaged over each meteorological season (3 months). Though averaging filters out short-term variations in wavenumber, it should capture long-term variability in the sea state, especially between winter and summer months in the Mellor–Yamada model. Further, variations in sea state due to storms which are not captured by the wavenumber averaging are largely reflected in the magnitude of the forcing Stokes drift. It is noted that in the derivation of the Ekman–Stokes kernel the waves are assumed to be deep-water waves, and therefore the wavenumber is calculated using the deep-water linear dispersion relationship, $\omega^2 = gk$. The peak wave period is an output parameter of the WaveWatch III hindcast.

2.4. Particle Tracking Simulations

In order to perform Lagrangian particle tracking simulations, we use Ocean Parcels (Probably a Really Computationally Efficient Lagrangian Simulator) (Delandmeter & Van Sebille, 2019) to advect virtual particles, representative of floating microplastics. To calculate the particle trajectories, Parcels uses the equation:

$$\boldsymbol{x}(t + \delta t) = \boldsymbol{x}(t) + \int_t^{t+\delta t} \boldsymbol{u}(\boldsymbol{x}(\tau), \tau)\,\mathrm{d}\tau, \tag{13}$$

where $\boldsymbol{x}(t)$ is the particle location at time t and $\boldsymbol{u}(\boldsymbol{x}(t), t)$ the flow field velocity at position $\boldsymbol{x}(t)$ and time t, which is calculated by linear interpolation. We perform Lagrangian simulations for 3 different flow field scenarios, which are

$$\boldsymbol{u} = \begin{cases} \boldsymbol{u}_{\mathrm{nwd}} = \boldsymbol{u}_{\mathrm{ek}} + \boldsymbol{u}_{\mathrm{geo}} & \text{Non-wave-driven (NWD) currents,} \\ \boldsymbol{u}_{\mathrm{nwd}} + \boldsymbol{u}_{\mathrm{s}} & \text{NWD currents} + \text{Stokes drift,} \\ \boldsymbol{u}_{\mathrm{nwd}} + \boldsymbol{u}_{\mathrm{s}} + \boldsymbol{u}_{\mathrm{wde}} & \text{NWD currents} + \text{Stokes drift} + \text{wave-driven Eulerian current,} \end{cases} \tag{14}$$

where $\boldsymbol{u}_{\mathrm{ek}}$ and $\boldsymbol{u}_{\mathrm{geo}}$ are the Ekman and geostrophic currents, respectively, and $\boldsymbol{u}_{\mathrm{wde}}$ the wave-driven Eulerian (WDE) current. We will further perform two separate wave-driven Eulerian current simulations corresponding to the constant viscosity and Mellor–Yamada model hindcast datasets, respectively. From this point onwards, the geostrophic + Ekman currents simulation will be known as the NWD currents simulation, the NWD currents + Stokes drift simulation will be known as the Stokes drift simulation, and the NWD currents + Stokes drift + WDE current simulations will be known as the constant viscosity and Mellor–Yamada simulations respectively. For each simulation the focus is solely on floating microplastics. Therefore all currents used are 2D, such that all virtual particles remain on the ocean surface, and 3D effects such as sinking or Ekman pumping are not considered. To integrate Equation 13, a fourth-order Runge-Kutta scheme is used with an integration time step of 30 min. All the simulations are run using the Globcurrent and WaveWatch III datasets and the calculated wave-driven Eulerian current datasets. All wavefields are processed at a 24 hr temporal resolution, by taking the daily mean for each 3-hourly data set. For the initial microplastic distribution, we use a homogeneous uniform distribution of particles at 1° intervals, equating to 35,145 particles for the global simulation. This is equivalent to that used by Onink et al. (2019) in his global Lagrangian experiments.

Finally, we also use an artificial shore-normal boundary current to prevent particles from beaching by pushing them away from the coast. This prevents virtual particles from getting stuck near the coast where no flow field data exists. The strength of the current is set to $1\ \mathrm{ms}^{-1}$ at points along coastlines where the flow field data is exactly equal to zero. This is necessary in order to effectively propel particles to a new location where they are then carried away by off-shore currents and is the same magnitude as used by Onink et al. (2019) and Sterl et al. (2020).

3. Results

Section 3.1 will first examine the local behaviors of the wave-driven Eulerian current hindcasts using a time series analysis, followed by a global analysis using flow field maps in Section 3.2. Section 3.3 presents the results of the Lagrangian particle tracking simulations.

3.1. Time Series

Having generated the wave-driven Eulerian current data, we extracted a month-long time series from each hindcast and examined the development of the Stokes drift, wave-driven Eulerian (WDE) current and (wave-induced) Lagrangian current at 2 points: in the North Atlantic at 45°N, 35°W and in the South Pacific at 30°S, 120°W. Figure 2 compares the magnitude of the forcing Stokes drift to the wave-driven Eulerian current and Lagrangian current at a 3-hourly and 24 hr daily averaged temporal resolution for both viscosity models. Comparing the temporal resolution of the plots, the time dependence of the Eulerian currents is clearly visible at the 3-hourly resolution as the complex transients oscillate, interfering constructively and destructively, with characteristic period ≈ 17 hr (Figures 2a, 2c, 2e and 2g). Averaging out the inertial oscillations, we can see that the daily averaged Eulerian current follows approximately the same shape as the forcing Stokes drift (Figures 2b, 2f, 2d and 2h).

The different viscosity models are compared in Figure 2 and Table 2. The Constant viscosity model ($\nu = 10^{-2}\ \mathrm{m^2 s^{-1}}$) produces a wave-driven Eulerian current which is 6% smaller in the North Atlantic and 8% smaller in the South Pacific than the forcing Stokes drift. Combining the wave-driven Eulerian current with the Stokes drift, the wave-driven Eulerian current has the effect of reducing the magnitude of the Lagrangian current by 16% and 22% respectively, as the Eulerian current acts in such a direction as to partially oppose the Stokes drift, Table 3. The
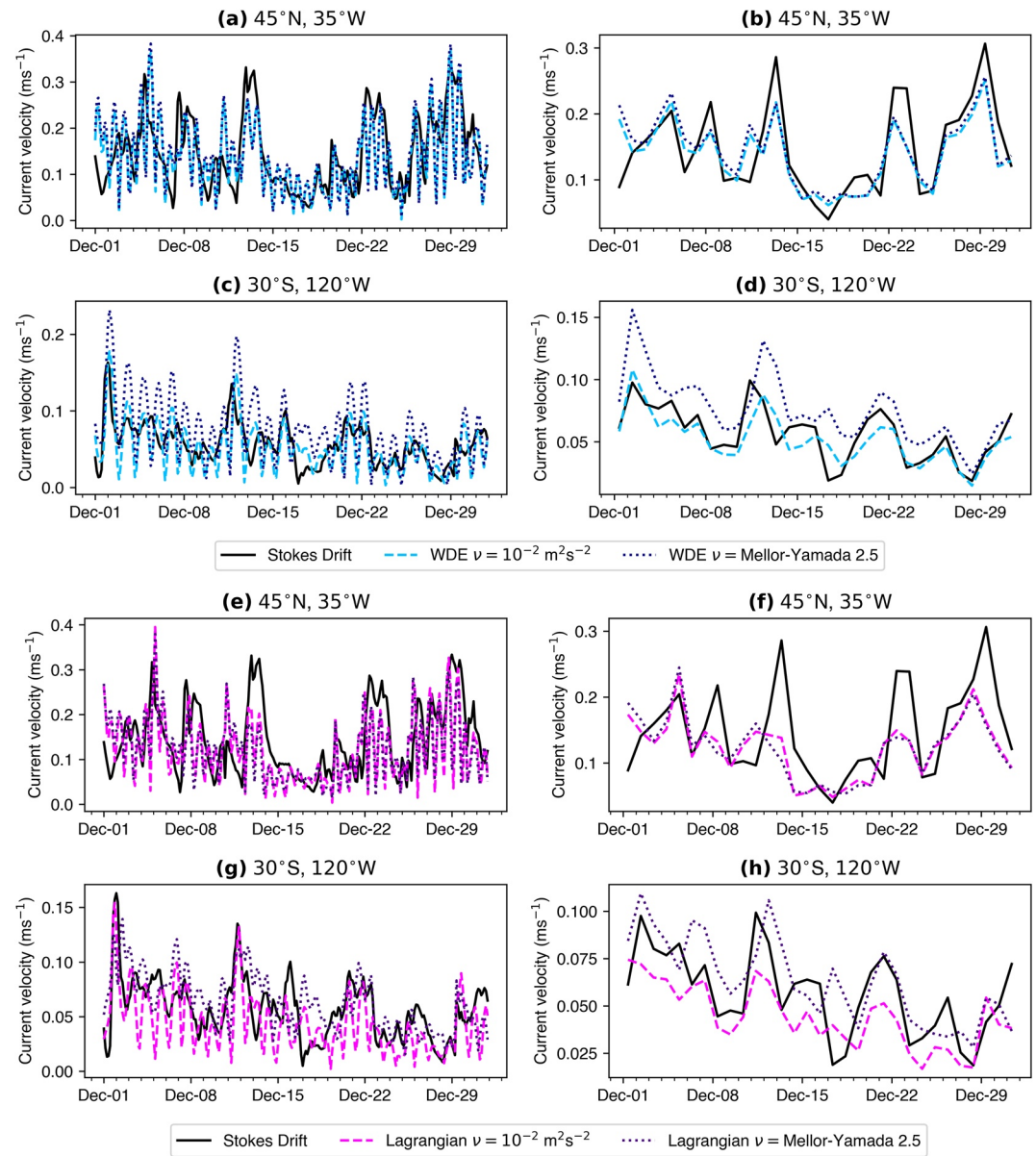
Figure 2. (a–d) Time series for the Stokes drift and wave-driven Eulerian current for both viscosity models during December 2002 (e–h) Time series for the Stokes drift and Lagrangian current ($\mathcal{U}_{\mathrm{L}} = \mathcal{U}_{\mathrm{S}} + \mathcal{U}_{\mathrm{E}}$) (a, c, e, and g) 3-hourly time series (b, d, f, and h) Daily averaged time series.

partial cancellation of the Stokes drift is as predicted by Madsen (1978), who showed that for any non-zero value of viscosity there is a non-zero mass transport associated with the Stokes drift in a rotating ocean, in contrast with the inviscid anti-Stokes result of Hasselmann (1970).

For the Mellor–Yamada viscosity model, the value of viscosity in the North Atlantic is 9×10^{-3} m^{2}s^{-1}, approximately equal to the value used in the Constant viscosity model. Consequently, the addition of the wave-driven Eulerian current to the Stokes drift also reduces the magnitude of the Lagrangian current by 16%. However, the eddy viscosity in the South Pacific is considerably smaller ($\nu = 2 \times 10^{-3}$ m^{2}s^{-1}). This has the effect of increasing the magnitude of the wave-driven Eulerian current by 34% of the magnitude of the Stokes drift, which in turn increases the magnitude of the Lagrangian current by 12%. This can be best understood by considering the kernel to be made up of two parts: the viscous $1/\sqrt{t}$ component which controls the development of the wave-driven spiral, and the *if* term which reflects the contribution of the Coriolis–Stokes forcing. Consequently,

Table 2

Analysis of the Wave-Driven Eulerian Current and Lagrangian Current Time Series at Two Chosen Points, and Then on Average Globally

Location	ν Model	ν (m²s⁻¹)	$\|\overline{\mathcal{U}_S}\|$ (m s⁻¹)	$\|\overline{\mathcal{U}_E}\|$ (m s⁻¹)	$\frac{\|\overline{\mathcal{U}_E}\|}{\|\overline{\mathcal{U}_S}\|}$	$\|\overline{\mathcal{U}_L}\|$ (m s⁻¹)	$\frac{\|\overline{\mathcal{U}_L}\|}{\|\overline{\mathcal{U}_S}\|}$
45°N, 35°W	Constant	1×10^{-2}	0.15	0.14	−6%	0.12	−16%
	M-Y 2.5	9×10^{-3}	0.15	0.14	−1%	0.12	−16%
30°S, 120°W	Constant	1×10^{-2}	0.06	0.05	−8%	0.04	−22%
	M-Y 2.5	2×10^{-3}	0.06	0.08	+34%	0.06	+12%
Global	Constant	1×10^{-2}	0.08	0.05	−35%	0.08	+4%
	M-Y 2.5	3×10^{-3}	0.08	0.05	−34%	0.07	−8%

the amplification of the current magnitude is in part due to the unsteady response of the wave-driven Eulerian current to the time-varying Stokes drift, as smaller values of viscosity reduce the amount of viscous damping in the *if* term of the kernel.

However, this increase in current magnitude does not necessarily lead to increased mass transport. In Table 3, the standard deviation of the change in angle between the Stokes drift and Lagrangian current, $\sigma^2_{\delta\theta_{\mathcal{U}_L}}$, increases with decreasing viscosity. This is an indication that the wave-driven Eulerian current has not yet reached steady state and also that it may be rotating with the local inertial frequency (e.g., Figures 3c, 3e and 3f). By contrast, for higher viscosities $\nu \approx 10^{-2}$ m²s⁻¹, panels a, b and c of Figure 3 show a definite directional signal as the wave-driven Eulerian current rotates the Lagrangian current by an angle between 0° and ∓90° to the Stokes drift in the Northern and Southern Hemispheres respectively. This equates to a |30–40°| change in angle on average between the Stokes drift and Lagrangian current, as shown by the global average change in angle, $\overline{\delta\theta_{\mathcal{U}_L}}$, for both models in Table 3. Indeed, for large values of viscosity the viscous $1/\sqrt{t}$ term dominates the behavior of the wave-driven Eulerian current, which isn't dependent on any viscous damping terms, and therefore the angle of the wave-driven Eulerian current converges much quicker to approximately the angle of the spiral term.

3.2. Global Maps

Averaging both wave-driven Eulerian current hindcasts for 1 year over 2002, we compare the wave-driven Eulerian current, Stokes drift and Lagrangian current flow fields.

Panels a, d, and e of Figure 4 illustrate how the addition of the wave-driven Eulerian current to the Stokes drift affects the Lagrangian current flow field. Looking first at the ocean circulation patterns of each current, the Stokes drift by itself (panel a) shows minimal convergence of ocean surface currents, with the direction of surface currents approximately aligning with the direction of the wind stress at the ocean surface. By contrast, if we look at the effect of the wave-driven Eulerian current on the Lagrangian current (panels d and e), there are notable areas of increased ocean circulation in all 5 major ocean basins as the WDE current acts to rotate the Lagrangian current around the ocean gyres. It must be noted however that, unlike wind-driven Ekman currents which do converge, the wave-driven Eulerian currents are non-convergent in our model, due to horizontal variation being neglected (e.g., Equation 1b). However, even without this higher-order Ekman–Stokes pumping, the Lagrangian current still exhibits behavior more normally associated with Ekman currents than the Stokes drift. This is consistent with the results of Polton et al. (2005), who showed how the Coriolis–Stokes forcing represents an effective change on the wind-driven Ekman current boundary condition, although they did not consider the surface wave stress.

Table 3

Analysis of the Wave-Driven Eulerian Current and Lagrangian Current Time Series at Two Chosen Points, and on Average Globally

Location	ν Model	ν (m²s⁻¹)	$\overline{\theta_{\mathcal{U}_S}}$	$\overline{\theta_{\mathcal{U}_E}}$	$\overline{\delta\theta_{\mathcal{U}_E}}$	$\sigma^2_{\delta\theta_{\mathcal{U}_E}}$	$\overline{\theta_{\mathcal{U}_L}}$	$\overline{\delta\theta_{\mathcal{U}_L}}$	$\sigma^2_{\delta\theta_{\mathcal{U}_L}}$
45°N, 35°E	Constant	1×10^{-2}	10°	217°	150°	22°	336°	40°	29°
	M-Y 2.5	9×10^{-3}	10°	204°	163°	25°	346°	32°	38°
30°S, 120°E	Constant	1×10^{-2}	248°	14°	−154°	19°	266°	−42°	30°
	M-Y 2.5	2×10^{-3}	248°	24°	179°	29°	327°	−1°	53°
Global	Constant	1×10^{-2}	-	-	|169°|	34°	-	|30°|	27°
	M-Y 2.5	3×10^{-3}	-	-	|161°|	33°	-	|39°|	32°

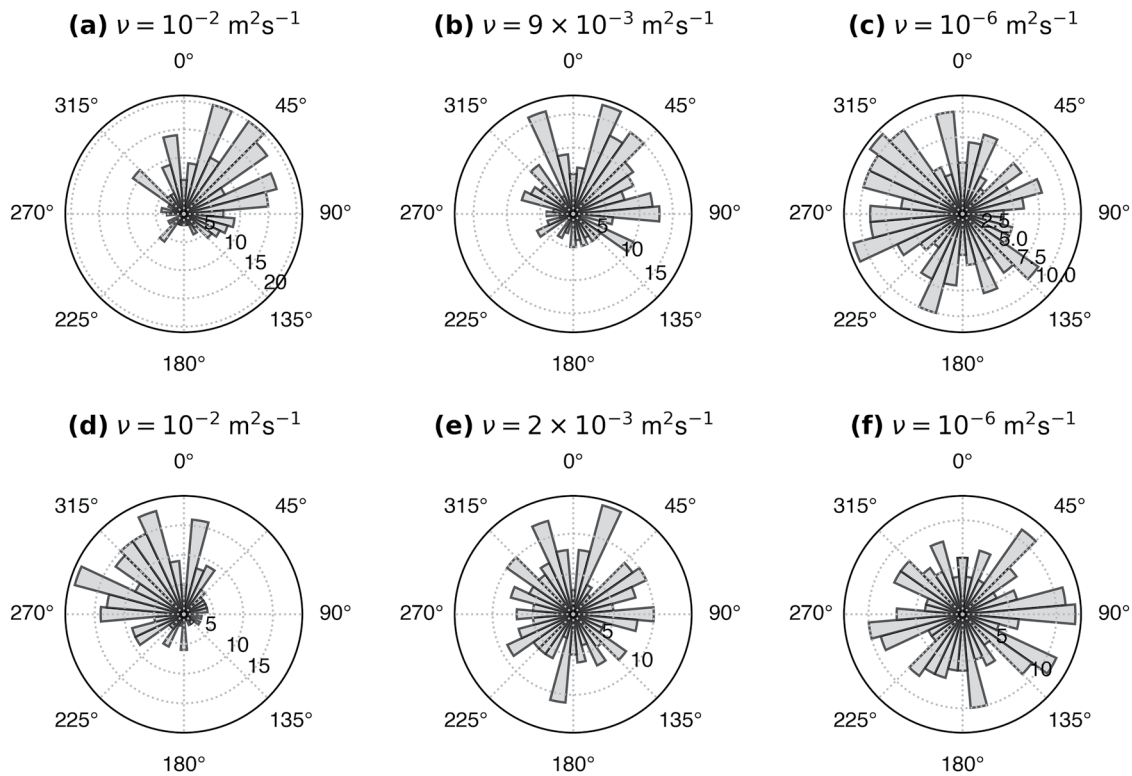*Note.* In order to calculate the global changes in angle in both Hemispheres, the absolute value is used.

Figure 3. Histograms, with 5° bins, of the difference in angle between the Stokes drift and the Lagrangian current $\left(\theta_{\nu_S} - \theta_{\nu_L}\right)$ (a–c) 45°N, 35°E (d,e,f) 30°S, 120°E. The case for $\nu = 10^{-6}$ m^{2}s^{-1} (The molecular viscosity of sea water) is provided as reference for when the viscous term is smallest, highlighting how the directional signal of the wave-driven Eulerian current is reliant on the value of viscosity.

Focusing attention to the tropics, the net result of reducing the value of viscosity to the molecular viscosity, is an amplification of the Lagrangian current by a factor ≈ 2 at the equator in both WDE models. This shows good agreement with the analytical solutions derived by (Longuet-Higgins, 1953), who concluded that the shear of the mass-transport velocity profile near the free surface is twice that predicted by Stokes' irrotational theory. Looking near the Equator in Figure 4, there are some clear differences between the two different viscosity models for the WDE current. Notably, the Constant viscosity model greatly amplifies the Lagrangian current in near-coastal areas, especially in the South China Sea and Gulf of Mexico. Comparing panels b and c of Figure 1, this is in part caused by the Constant viscosity model overestimating the value of the eddy viscosity in these regions by an order of magnitude compared to the Mellor–Yamada model, which better resolves near-coastal currents. Consequently, the Mellor–Yamada model exhibits smaller areas of boundary layer streaming, reflecting the more realistic lower values of eddy visocity in the tropics.

The direction of the Lagrangian current is also altered significantly in the equatorial band and the subtropics. Whereas the Stokes drift either side of the Equator naturally flows in an eastward direction, aligning with the direction of the prevailing easterly trade winds, both wave-driven Eulerian current models exhibit a divergent-like behavior, notably in the Pacific Ocean, where currents flow perpendicular to and away from the Equator. This is due to the reduction of the Coriolis–Stokes forcing at low latitudes as $f \to 0$, causing the Eulerian current to no longer oppose the Stokes drift but instead act to enhance it, leading to boundary layer streaming (Longuet-Higgins, 1953). The large change of direction that accompanies boundary layer streaming reveals interesting current behaviors in the zonal regions where the angular deflections are largest. Indeed, the largest changes in angle occur at the onset of boundary layer streaming, when the displacement caused by the viscous term acts at $\approx 90°$ to the Stokes drift at $\approx \pm 30°$ latitude in the subtropics. This is significant, since microplastic accumulation zones are found in the subtropical ocean gyres which occur at approximately $\pm 30°$ latitude.

The bending of the Lagrangian current in the subtropics to better align with Ekman currents is likely to increase the amount of material accumulating in the subtropical ocean gyres, counteracting the dispersive behavior of the
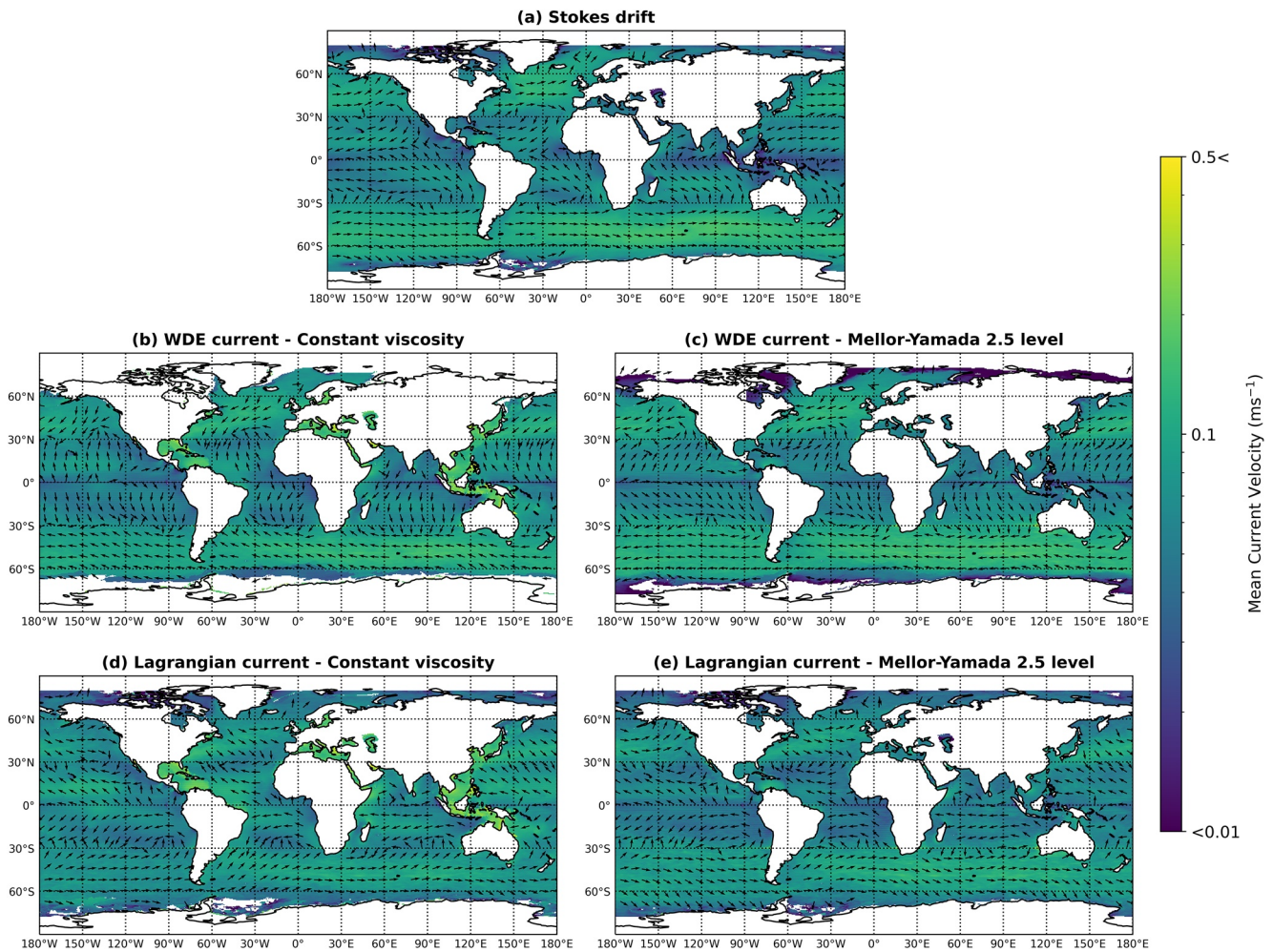
Figure 4. Mean flow field maps averaged over 2002, for the Stokes drift, wave-driven Eulerian current (WDE) and the Lagrangian current for the Constant viscosity model (b and d) and the Mellor–Yamada 2.5 level viscosity model (c and e). The vectors indicate the mean direction of the flow and the colormap indicates the current magnitude. Note the scale is logarithmic.

Stokes drift. Both models exhibit the bending of currents in the subtropics, however the Mellor–Yamada model does not deflect the currents as much as the Constant viscosity model, in keeping with the results of the time series analysis in Table 3. In contrast, away from the equatorial band and into high-latitude regions where the Coriolis parameter is larger, we expect to see smaller angles of deflection as the Coriolis–Stokes forcing term of the Ekman–Stokes kernel dominates over the viscous term. Consequently, the directional preference of the WDE current is weaker (cf. Figure 3). At these latitudes, the magnitude of the Lagrangian current in both cases is $\approx 80\%$ of the Stokes drift. Both current models deflect the Lagrangian current differently, as the larger viscosity used in the Constant viscosity model causes the viscous term of the Ekman–Stokes kernel to dominate and the WDE current to rotate the Lagrangian current away from the Antarctic regions and back toward the subtropics.

The wave-driven Eulerian current therefore, has a pronounced effect on the Lagrangian current, acting to both increase the magnitude and alter the direction of the Lagrangian current in the equatorial band and subtropics, and oppose the Stokes drift in higher-latitude and polar regions.

3.3. Lagrangian Simulations

Performing particle tracking simulations over a 12-year period between 2002 and 2014 for each of the flow field scenarios in Equation 14, we note from Figure 5 the presence of microplastic accumulation zones in all scenarios. Similar to Onink et al. (2019), the microplastic distributions reach steady state after 8 years and are approximately
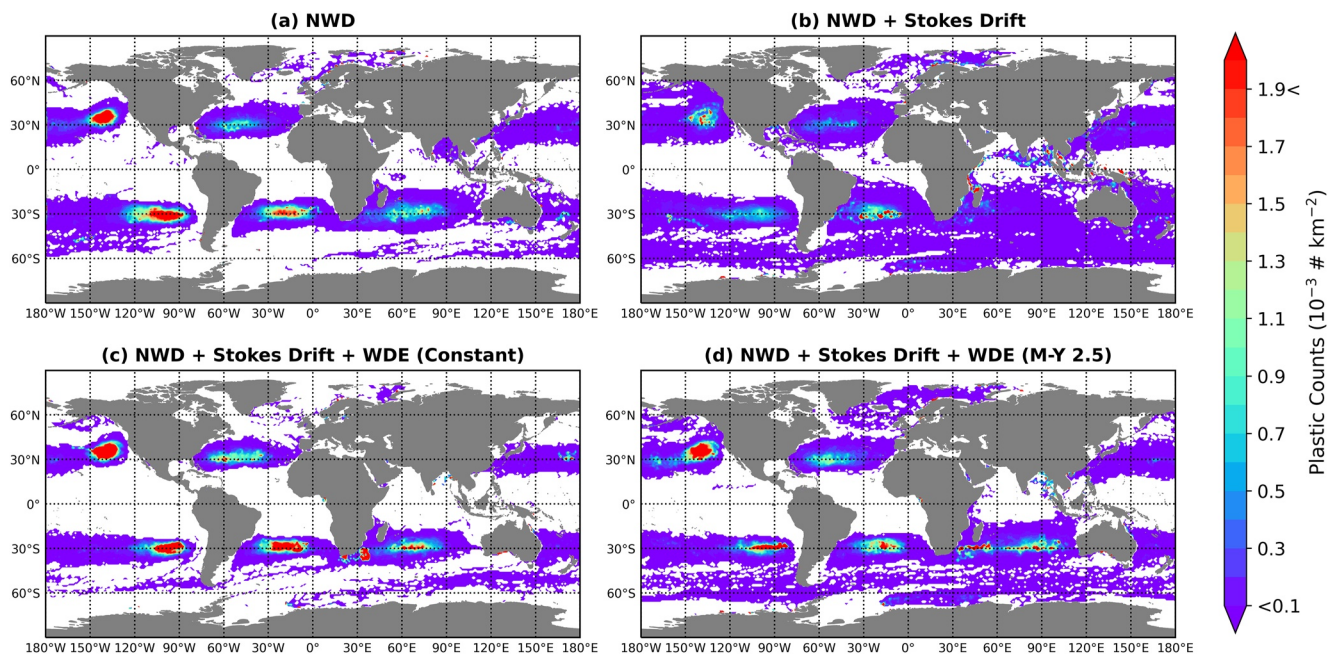
Figure 5. The average particle density for the final year of the global Lagrangian simulations with the virtual particles advected by: NWD currents (a), NWD currents + Stokes drift (b), NWD + Stokes drift + wave-driven Eulerian (WDE) (c and d). Simulations are from 01-01-2002 to 31-12-2014 from an initial uniform $1° \times 1°$ distribution of particles.

stationary over the final 4 years of the simulation. The formation of these accumulation zones is largely attributed to the convergence of surface Ekman currents (Kubota, 1994; Kubota et al., 2005; Law et al., 2014; Maximenko et al., 2012), but is also affected by surface waves and geostrophic currents. In the NWD current simulation (Figure 5a), the addition of geostrophic currents counteracts microplastic accumulation, more widely dispersing particles across the subtropics than those formed by pure Ekman convergence (Onink et al., 2019).

Superimposing the Stokes drift with the NWD currents further disperses microplastics from the subtropics across the tropics and toward the poles, Figure 5b. Summarizing the results of Onink et al. (2019), Stokes drift has a strong influence on inter-basin connectivity, transporting particles westwards in the Southern Hemisphere. These results are well-reflected in Figure 6b in the westward stretching of ocean basins and the westward transportation of microplastics to the South Atlantic, causing the disappearance of the Indian Ocean accumulation zone Figure 5b. As a result, in the Stokes drift simulation we find a 254% increase in the number of particles which cross the Equator and are found in the opposite hemisphere to their starting location.

The Stokes drift also increases particle accumulation in the polar regions. We see a 218% increase in the number of particles in the Southern Ocean basin in the Stokes drift simulation compared to the NWD currents simulation. In the Arctic Ocean the increase in microplastic accumulation is due to elevated transport from the North Atlantic, whose loss of plastics is balanced by increased northward transport across the Equator from the South Atlantic. It is important to note that, as expected, the numerical results from the Stokes drift simulation are in strong agreement with those of Onink et al. (2019).

The addition of the wave-driven Eulerian current with the NWD currents and Stokes drift significantly alters the accumulation patterns and pathways of floating microplastics in different ways for both viscosity models. Focusing again on the behavior of the wave-driven Eulerian current flow fields in Figure 4 (panels b and c), whilst the circulation patterns in both viscosity models look similar - both WDE currents flow easterly in low southerly latitudes and exhibit greater circulation in the subtropics - there are notable differences in their respective effects on the Lagrangian current, causing different accumulation dynamics. From Figures 5c and 5d, it is clear that both wave-driven Eulerian current simulations do indeed produce areas of dense microplastic accumulation in all 5 subtropical ocean gyres. However, the action of the WDE current in the constant viscosity simulation, Figures 5c and 5d is to almost entirely reverse the dispersive effects of the Stokes drift, such that almost all of the input microplastics accumulate in the subtropics. In the Mellor–Yamada simulation, Figure 5d, this reduction of the
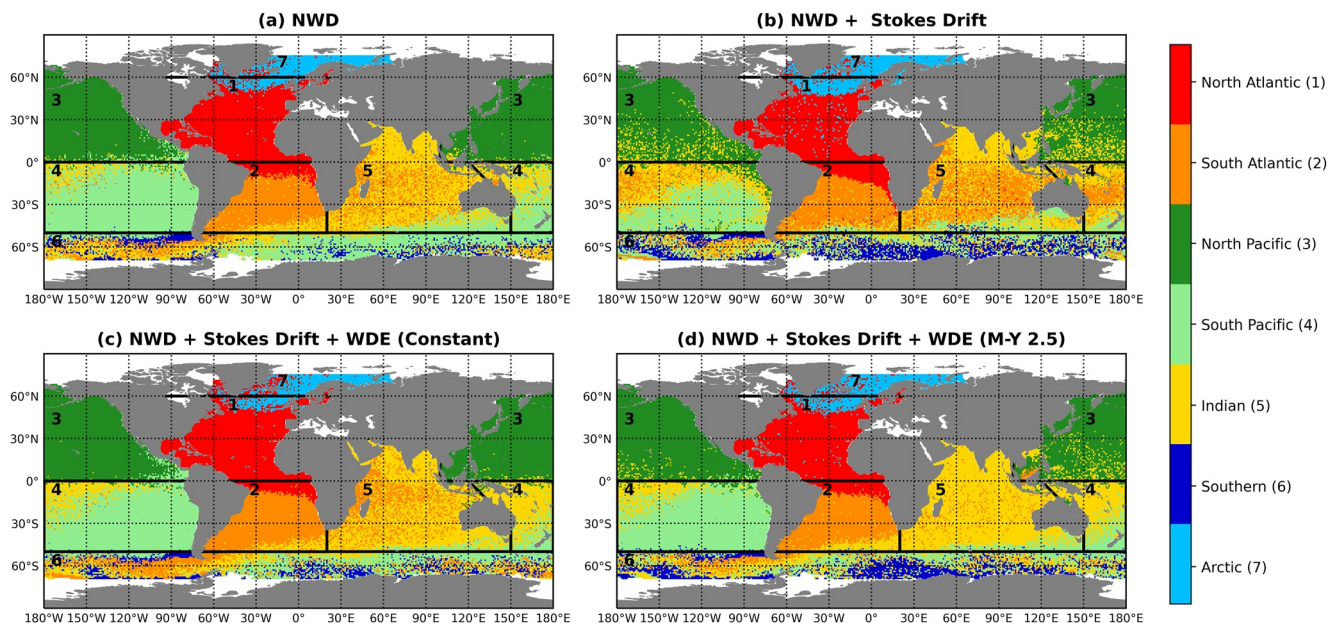
Figure 6. Inter-basin connectivity of particles for the 4 Lagrangian simulation scenarios. Particles are shown at their initial position and are colored according to their final position at the end of the simulation.

dispersive impact of the Stokes drift is less pronounced, whilst the microplastic accumulation zones are smaller and more concentrated. Further, both the Stokes drift simulation and Mellor–Yamada simulation exhibit large areas of dispersion beneath the subtropics and in the polar regions, unlike in the constant viscosity simulation. However, unlike the Stokes drift simulation, the Mellor–Yamada simulation produces a clear accumulation zone in the Indian Ocean.

Examining the accumulation of microplastics in the equatorial band, Figures 5c and 5d show how the addition of the wave-driven Eulerian current clears the tropics of microplastics. Focusing on the South China Sea and Bay of Bengal in Figure 5c, there are no obvious areas of microplastic accumulation, differing markedly to Figures 5a and 5b, which show clear accumulation in the Bay of Bengal and off the coast of Indonesia for simulations without any wave-driven Eulerian currents. Coupled with the divergent-like behavior of the Lagrangian current near the Equator in Figure 4, this suggests that the wave-driven Eulerian current has a significant effect on the ability of microplastics to cross the equator. Indeed, the inclusion of the Mellor–Yamada wave-driven Eulerian current causes a 45% reduction in particles whose final location is in the opposite hemisphere to their starting location, compared to the Stokes drift simulation. It must be noted that the amount of cross-Equator transport governed by the wave-driven Eulerian current is sensitive to the value of viscosity. For instance, the Indian Ocean in the Mellor–Yamada simulation received 8 times as many particles from the North Pacific when compared to the constant viscosity simulation, albeit still 59% less than in the Stokes drift simulation. As noted above, this is due to the Mellor–Yamada model retaining some dispersive action of the Stokes drift. Hence, while the wave-driven Eulerian current inhibits particle transport across the equatorial band, cross-Equator transport pathways are dependent on the value of viscosity.

The effect of the wave-driven Eulerian current on the transport of microplastics to the polar region is also sensitive to the value of viscosity. The addition of the wave driven Eulerian current reverses some of the increased microplastic transport to the Arctic Ocean, especially in the constant viscosity simulation, where the number of particles present in the Arctic Ocean at the end of the simulation is 29% less than in the Stokes drift simulation. The Mellor–Yamada simulation also reduces the number of particles present in the Arctic Ocean by 17% compared to the Stokes drift simulation, though unlike the Constant viscosity model, the amount of poleward transport compared to the NWD currents simulation is still increased by 5%. The effects of the wave-driven Eulerian current are visible in Figures 5c and 5d, as there are no clear patches of dense microplastic accumulation in the Arctic Ocean but the Mellor–Yamada simulation in Figure 5d clearly shows greater dispersion across the Arctic basin. Differences between the two wave-driven Eulerian simulations are also apparent in the Southern

Ocean. In the constant viscosity simulation, the proportion of particles originating in the Southern Ocean that are present in the South Atlantic at the end of the simulation rose by 15%, reversing the poleward travel of particles seen in the Stokes drift simulation. The behavior differs in the Mellor–Yamada simulation, in which the wave-driven Eulerian current behaves similarly to the Stokes drift in the Southern Ocean, increasing the number of particles retained within the basin throughout the simulation by 79% compared to the NWD currents simulation and increasing the amount of poleward particle transport from the South Pacific to the Southern Ocean. Consequently both wave-driven Eulerian currents behave markedly different, as the constant viscosity simulation acts to accumulate particles in the subtropics, whilst the Mellor–Yamada simulation retains the poleward transport of microplastics caused by the Stokes drift.

The wave-driven Eulerian current also has a strong influence on inter-basin connectivity in the Southern Hemisphere. Stokes drift increases the connectivity of ocean basins, particularly in the Southern Hemisphere as around half of all particles in the South Pacific, South Atlantic and Indian basins are found in a different ocean basin than their point of origin (Onink et al., 2019). Retention rates of particles originating in the Southern Hemisphere subtropical ocean basins are considerably increased when the WDE current is superimposed, most notably in the Indian Ocean where, in the Mellor–Yamada simulation, 78% more particles are retained in the basin compared to the Stokes drift simulation (cf. Table 4). This effect is seen quite clearly in the reduced particle mixing in the Southern Hemisphere basins in Figures 6c and 6d compared to the Stokes drift simulation in Figure 6b. This result is arguably foreshadowed in Figure 4, where the addition of the wave-driven Eulerian current causes increased ocean circulation in the subtropical ocean gyres and closer alignment with traditional Ekman dynamics, suggestive of increased microplastic accumulation.

3.4. Comparison With Observed Distributions

We compare our modeled microplastic distributions with observed distributions in the North Pacific and North Atlantic, using observational microplastic data gathered by van Sebille et al. (2015) and presented in (Onink et al., 2019). As highlighted by Onink et al. (2019) the North Pacific and North Atlantic are the only regions with a meaningfully high number of observational data points.

Examining Figure 7, the addition of the Stokes drift to the NWD currents does not lead to closer agreement between the modeled and observed microplastic distributions, in accordance with the results of Onink et al. (2019). In the North Pacific we see that the addition of the Stokes drift to the NWD currents flattens the peak concentration in the subtropics due to strong dispersion of particles Northwards toward the Arctic, highlighted by the northerly peaks in concentration between 50° and 65°N in Figure 7d. In the North Atlantic, the Stokes drift has the effect of dispersing the accumulation zone over a larger area, seen by the similar shape to the NWD simulation but lower concentrations across the subtropics.

The addition of the WDE current, however, does lead to closer agreement between the observed and modeled microplastic distributions. In the North Pacific both viscosity models show increased peaks in concentration at 35°N and 140°W when compared to the NWD simulations, aligning better with the higher concentration peaks seen in the observed microplastic distribution. Further, both WDE current models also show very low microplastic concentrations in the equatorial band, in strong agreement with the observed distribution (Figure 7d). The increased peak concentrations at the center of the accumulation zones and reduced concentration in the equatorial band are indicative of increased microplastic accumulation in the subtropics driven by WDE currents. Both WDE viscosity models also show increased microplastic transport to the polar regions in the North Pacific, though reduced compared to the Stokes drift simulation, again contributing to increased microplastic concentration in the subtropics when compared with the Stokes drift simulation (Figure 7d).

In the North Atlantic the addition of the WDE current again leads to closer alignment between modeled and observed microplastic distributions. Zonally, the addition of the constant viscosity and Mellor-Yamada WDE currents produce higher peaks in concentration at 30°N, increasing the alignment with the observed peak concentrations and further emphasizing the role the WDE current has on increasing microplastic accumulation in the subtropics (Figure 7b). In the meridional direction the WDE current simulations lead to a general increase in concentration across the center of the ocean basin, compared to the NWD simulation. The addition of the WDE current also results in clear bimodal peaks, the second of which at 45−40°W is ≈5° east of the observed peak

Table 4
Global Statistics Describing the Composition of Microplastics in a Given Ocean Basin at the End of the 14-Year Simulation, Given the Basin of Origin of the Particles

Basin of origin	North Atlantic				South Atlantic				North Pacific				South Pacific			
	N	N + S	N + S + E1	N + S + E2	N	N + S	N + S + E1	N + S + E2	N	N + S	N + S + E1	N + S + E2	N	N + S	N + S + E1	N + S + E2
North Atlantic	83.5%	77.2%	82.3%	82.8%	-	-	-	-	-	-	-	-	-	-	-	-
South Atlantic	12.5%	17.1%	11.1%	12.5%	49.1%	33.6%	43.2%	62.2%	-	-	-	-	0.1%	2.2%	2.3%	0.3%
North Pacific	-	-	-	-	0.3%	0.2%	-	-	97.3%	92.5%	96.6%	96%	1.9%	-	-	0.5%
South Pacific	-	-	-	-	1.6%	17.0%	0.7%	1.9%	2.1%	6.2%	2.1%	2.9%	57.0%	45.8%	61.7%	65.6%
Indian	-	1.4%	-	-	31.2%	37.7%	29.4%	12%	0.6%	1.2%	1.3%	1.1%	7.0%	11.5%	3.8%	6.2%
Southern	-	0.3%	-	-	17.8%	11.6%	26.7%	23.4%	-	0.2%	-	-	33.9%	40.6%	32.2%	27.3%
Arctic	3.9%	4.0%	6.6%	4.7%	-	-	-	-	-	-	-	-	-	-	-	-
Total particles	4,289	4,211	4,367	4,213	4,628	6,174	5,616	3,582	7,452	6,706	7,592	7,199	9,379	5,439	7,468	7,115

Basin of origin	Indian				Southern				Arctic			
	N	N + S	N + S + E1	N + S + E2	N	N + S	N + S + E1	N + S + E2	N	N + S	N + S + E1	N + S + E2
North Atlantic	-	-	-	-	-	-	-	-	29.7%	44.1%	32.0%	35.1%
South Atlantic	5.5%	3.3%	3.7%	4.3%	-	0.3%	-	0.3%	-	-	-	0.2%
North Pacific	1.8%	16.1%	0.9%	5.8%	-	-	-	-	-	-	-	-
South Pacific	16.0%	31.9%	24.4%	18.5%	0.9%	1.7%	0.4%	1.7%	-	-	-	-
Indian	54.8%	33.1%	50.7%	52.1%	0.3%	2.3%	0.2%	0.7%	-	0.1%	-	-
Southern	21.9%	15.5%	19.8%	19.3%	98.9%	95.6%	99.4%	97.3%	-	-	-	-
Arctic	-	-	-	-	-	-	-	-	70.3%	55.8%	68.0%	64.7%
Total particles	6,927	8,445	7,711	9,552	1,159	2,524	1,246	2,104	1,276	1,611	1,145	1,345

Note. N = NWD Currents, S = Stokes Drift, E1 = Wave-Driven Eulerian Current (Constant Viscosity Model), E2 = Wave-Driven Eulerian Current (Mellor–Yamada Viscosity Model).
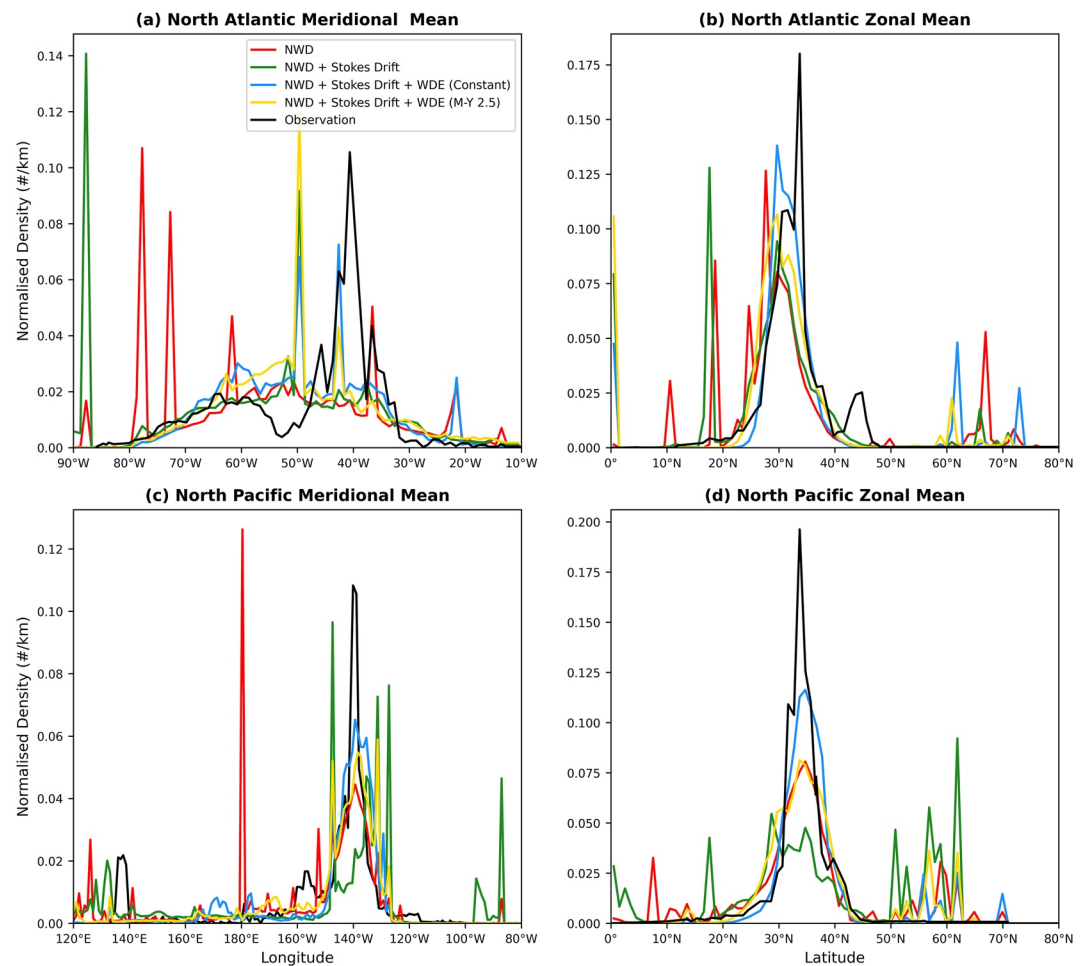
Figure 7. Comparison between normalized zonal and meridional means of modeled and observed (Onink et al., 2019; van Sebille et al., 2015) microplastic distributions for (a and b) the North Atlantic and (c and d) the North Pacific. For the North Atlantic the means are computed over the area 90° to 10°W (meridional) and 0° to 80°N (zonal). For the North Pacific the means are computed over the area 120°E to 90°W (meridional) 0° to 80°N (zonal). All curves are normalized individually such that the area under each curve is equal to 1 (Onink et al., 2019).

in concentration. Although no bimodal peak is visible in the observed distribution, there is no similar peak in concentration at 40°W in the Stokes drift simulation.

It should be noted that toward the edges of both ocean basins, the simulated distributions are susceptible to artificial peaks in concentration due to particles getting stuck near coastlines. This is particularly true for the westward peaks in microplastic concentrations in the North Atlantic (Figure 7a), due to particles getting stuck near the Caribbean and northwards of 60°N latitude in the polar regions (Figures 7b and 7d).

4. Discussion and Conclusions

This paper has demonstrated the need to include the wave-driven Ekman–Stokes Eulerian current in order to better estimate the accumulation dynamics of floating marine litter, in particular microplastics. We have implemented the convolution kernel derived by Higgins et al. (2020) to create a 12-year global hindcast for two different viscosity models: a temporally and spatially constant viscosity model, and a spatially varying and quasi-stationary viscosity model derived using the Mellor–Yamada 2.5 level turbulence closure model. Having generated the hindcast datasets, we superimpose the wave-driven Eulerian current with NWD currents and the Stokes drift before performing four different particle tracking simulations over a 12-year period between 2002 and 2014.

In Section 3, we showed that the addition of the wave-driven Eulerian current affects the distribution and accumulation dynamics of floating microplastics in different ways, showing better agreement with observed microplastic densities. In the constant viscosity simulation, the combination of reduced transport toward the poles and clearing of microplastics in the tropics is evidence of increased microplastic accumulation in the subtropics. On the other hand, whilst the Mellor–Yamada simulation also reduces cross-Equator particle transport, it retains some of the dispersive action of the Stokes drift, causing increased particle transport to the polar regions when compared to the NWD current simulation. Both wave-driven Eulerian currents also increase the retention rate of particles in each Southern Hemisphere subtropical ocean basin. The remainder of this section will discuss what causes the differences in behavior between the models.

First, while the Stokes drift acts to increase inter-basin connectivity, the wave-driven Eulerian current works to retain particles in the subtropical ocean basins, resulting in dense areas of microplastic accumulation at the center of each ocean gyre. This is due to the wave-driven Eulerian current significantly deflecting the Lagrangian current from the Stokes drift at approximately $\pm 30°$ latitude, causing enhanced ocean circulation in the subtropics. This is initiated by the amplification of the viscous term at a near-perpendicular angle to the Stokes drift, leading to large changes in the angle of the Lagrangian current with respect to the Stokes drift. Consequently, the behavior of the wave-driven Eulerian current in the subtropics is sensitive to the value of viscosity, as seen in the differing flow field patterns in Figures 4d and 4e. The results of the time-series analysis in Section 3.1 further reflects how the complex interactions between the viscous and Coriolis terms of the kernel are dependent on the viscosity model used, and this choice of model can result in significant changes to the current magnitude and spread of angular deflections. Indeed, the smaller values of viscosity in the subtropics when using the Mellor–Yamada model cause the wave-driven Eulerian current to rotate the Lagrangian current less compared to the Constant viscosity model. Consequently, the Mellor–Yamada viscosity simulation retains some of the dispersive action of the Stokes drift.

The transport dynamics under both viscosity models also differ significantly in the polar regions. While the constant viscosity simulation results in reduced microplastic transport to the poles, the Mellor–Yamada viscosity simulation still shows increased microplastic transport to the Arctic and Southern Oceans when compared to the NWD currents simulation. The results of the Mellor–Yamada viscosity simulation are significant, as they largely support the findings by Onink et al. (2019) and Fraser et al. (2018) which show increased transport to the Arctic and Antarctic due to the effect of the Stokes drift. Transportation of microplastics to the poles by the wave-driven Eulerian current is caused by the bending of the Lagrangian current in high zonal regions due to the dominant Coriolis term in the kernel convolution. Here, the wave-driven Eulerian current behaves much more like an anti-Stokes current, opposing the direction of the Stokes drift and reducing the magnitude of the Lagrangian current. The effect of this is that the Stokes drift, driven by prevailing westerly winds in the Southern Hemisphere, is rotated clockwise by the wave-induced Eulerian current for small values of viscosity and microplastics are transported to the Southern Ocean. Conversely, for larger values of viscosity such as in the Constant viscosity model, the viscous term is still important, bending the currents anticlockwise toward the subtropics.

Finally, the wave-driven Eulerian current opposes cross-equatorial transport by counteracting the effects of the Stokes drift. This effect is driven by boundary layer streaming in the equatorial band which causes particles to be transported away from the Equator, evacuating the Bay of Bengal and South China Sea of microplastics. Without any rotation to drive Ekman–Stokes dynamics, surface microplastics don't experience the large eddy viscosity values within the mixed layer. In order to control large amplifications of the Lagrangian current due to boundary-layer streaming (see e.g., Longuet-Higgins (1953); Grue and Kolaas (2017)) near the Equator where $f \to 0$, we linearly reduced the eddy-viscosity value at $\pm 20°$ latitude to the molecular value of seawater, $\nu = 1 \times 10^{-6}$ m^{2}s^{-1}, at the Equator. Though this reduction toward molecular viscosity is a somewhat artificial correction, it represents an alternative to ignoring the Equatorial band entirely, as is common in the literature (Hui & Xu, 2016; McWilliams & Restrepo, 1999).

5. Recommendations and Further Work

Several challenges arise when trying to model both the global ocean flow field and the accumulation dynamics of ocean currents using Lagrangian simulations. We examine these in turn.

First, the current datasets may not be fully independent: it has already been mentioned in Section 2.2 that the Globcurrent and WaveWatch III datasets are not truly independent due to the incomplete removal of ageostrophic

noise. The angle of the surface Ekman currents from the Globcurrent data set also differs from theoretical Ekman currents, acting at angles between 30 and 40° to the surface wind stress. Whilst it is inevitable that discrepancies exist between theory and observed currents, there is a possibility that some of the WDE currents may already be included in the Ekman current datasets. Possible non-independence of the Ekman and WDE datasets could lead to overestimation of the WDE current, contributing to unexplained differences in the deflection angle of surface Ekman currents.

Second, the treatment of the wavenumber is also important. We have assumed that the peak wave frequency and hence the wavenumber will remain approximately constant about its mean value. This removes much of the wavenumber's temporal variation, though we allow for seasonal variation by averaging the peak wave frequency every 3 months before calculating the wavenumber using the deep-water linear dispersion relationship. This treatment neglects wave refraction by currents and non-linear evolution of the wave spectrum, which may lead to errors in the direction of transport associated with swell seas (Gallet & Young, 2014) and underestimation of the impact of Langmuir circulations (Onink et al., 2019).

Though we have taken the wave spectrum to be monochromatic for the sake of simplicity, we note that the Ekman–Stokes convolution may be adapted for a broadbanded spectrum by adding an additional outer integral over the wavenumber k. Since better approximations of the Stokes drift depth profile for a broadbanded sea can be inferred from the wave spectrum (e.g., Breivik et al. (2014)), future work should also consider the effect of alternative Stokes drift depth profiles on the wave-driven Eulerian current.

Third, the divergence of the surface wave stress should induce a weak vertical velocity, analogous to the wind-driven Ekman pumping, which would result in regions of upwelling where waves diverge and downwelling where waves converge. Though the divergence of the wave stress is likely to be weak in general, this upwelling may influence the zones of microplastic convergence, notably at higher latitudes where wave activity is generally greatest (see, Figure 4d and 4e).

Finally, given the lack of observational data concerning the evolution and distribution of global accumulation zones, it is difficult to verify the modeled results of the Lagrangian simulations. Lagrangian tracking simulations, such as those contained in this work and the review by Sebille et al. (2018), are improving agreement between modelled and observed microplastic distributions, but sampling efforts need to be expanded globally before any definitive evaluations on the quality of modelled microplastic distributions can be made.

Data Availability Statement

GlobCurrent data can be found at: http://www.ifremer.fr/opendap/cerdap1/globcurrent/v3.0/, WaveWatch III hindcast data at: ftp://ftp.ifremer.fr/ifremer/ww3/HINDCAST/GLOBAL/ and the NOAA blended surface wind stress at: https://data.noaa.gov/dataset/dataset/noaa-ncdc-blended-daily-0-25-degree-sea-surface-wind-stress1. Observed microplastic data is found at: https://doi.org/10.6084/m9.figshare.17427572.v1. The wave-driven Eulerian current datasets generated in this paper for the constant viscosity model and Mellor-Yamada 2.5 viscosity model are available at https://doi.org/10.6084/m9.figshare.18134687 and https://doi.org/10.6084/m9.figshare.18135077 respectively. Code used to run the experiments and create the figures for this publication can be found at the Github repository https://github.com/HJakeCunningham/Microplastics.

References

Ardhuin, F., Marié, L., Rascle, N., Forget, P., & Roland, A. (2009). Observation and estimation of Lagrangian, Stokes, and Eulerian currents induced by wind and waves at the sea surface. *Journal of Physical Oceanography*, *39*(11), 2820–2838.

Breivik, Ø., Janssen, P. A., & Bidlot, J.-R. (2014). Approximate Stokes drift profiles in deep water. *Journal of Physical Oceanography*, *44*(9), 2433–2445.

Cózar, A., Echevarría, F., González-Gordillo, J. I., Irigoien, X., Úbeda, B., Hernández-León, S., et al. (2014). Plastic debris in the open ocean. *Proceedings of the National Academy of Sciences*, *111*(28), 10239–10244. https://doi.org/10.1073/pnas.1314705111

Craik, A. D., & Leibovich, S. (1976). A rational model for Langmuir circulations. *Journal of Fluid Mechanics*, *73*(3), 401–426.

Delandmeter, P., & Van Sebille, E. (2019). The parcels v2. 0 Lagrangian framework: New field interpolation schemes. *Geoscientific Model Development*, *12*(8), 3571–3584.

Dobler, D., Huck, T., Maes, C., Grima, N., Blanke, B., Martinez, E., & Ardhuin, F. (2019). Large impact of Stokes drift on the fate of surface floating debris in the South Indian Basin. *Marine Pollution Bulletin*, *148*, 202–209. https://doi.org/10.1016/j.marpolbul.2019.07.057

Eriksen, M., Lebreton, L., Carson, H., Thiel, M., Moore, C., Borerro, J., et al. (2014). Plastic pollution in the world's oceans: More than 5 trillion plastic pieces weighing over 250,000 tons afloat at sea. *PLoS ONE*, *9*(12).

Fraser, C. I., Morrison, A. K., Hogg, A. M., Macaya, E. C., van Sebille, E., Ryan, P. G., et al. (2018). Antarctica's ecological isolation will be broken by storm-driven dispersal and warming. *Nature climate change*, *8*(8), 704–708.

Gallet, B., & Young, W. (2014). Refraction of swell by surface currents. *Journal of Marine Research*, *72*(2), 105–126.

Grue, J., & Kolaas, J. (2017). Experimental particle paths and drift velocity in steep waves at finite water depth. *Journal of Fluid Mechanics*, *810*, R1. https://doi.org/10.1017/jfm.2016.726

Hardesty, B. D., Harari, J., Isobe, A., Lebreton, L., Maximenko, N., Potemra, J., et al. (2017). Using numerical model simulations to improve the understanding of micro-plastic distribution and pathways in the marine environment. *Frontiers in Marine Science*, *4*, 30.

Hasselmann, K. (1970). Wave-driven inertial oscillations. *Geophysical and Astrophysical Fluid Dynamics*, *1*(3-4), 463–502.

Higgins, C., Vanneste, J., & van den Bremer, T. S. (2020). Unsteady ekman-stokes dynamics: Implications for surface wave-induced drift of floating marine litter. *Geophysical Research Letters*, *47*(18), e2020GL089189. https://doi.org/10.1029/2020GL089189

Huang, N. E. (1979). On surface drift currents in the ocean. *Journal of Fluid Mechanics*, *91*(1), 191–208.

Hui, Z., & Xu, Y. (2016). The impact of wave-induced Coriolis-Stokes forcing on satellite-derived ocean surface currents. *Journal of Geophysical Research: Oceans*, *121*(1), 410–426.

Iwasaki, S., Isobe, A., Kako, S., Uchida, K., & Tokai, T. (2017). Fate of microplastics and mesoplastics carried by surface currents and wind waves: A numerical model approach in the Sea of Japan. *Marine Pollution Bulletin*, *121*(1-2), 85–96.

Kubota, M. (1994). A mechanism for the accumulation of floating marine debris north of hawaii. *Journal of Physical Oceanography*, *24*(5), 1059–1064.

Kubota, M., Takayama, K., & Namimoto, D. (2005). Pleading for the use of biodegradable polymers in favor of marine environments and to avoid an asbestos-like problem for the future. *Applied Microbiology and Biotechnology*, *67*(4), 469–476.

Law, K., Morét-Ferguson, S., Goodwin, D., Zettler, E., Deforce, E., Kukulka, T., & Proskurowski, G. (2014). Distribution of surface plastic debris in the Eastern Pacific Ocean from an 11-year data set. *Environmental science & technology*, *48*(9), 4732.

Lewis, D., & Belcher, S. (2004). Time-dependent, coupled, Ekman boundary layer solutions incorporating Stokes drift. *Dynamics of atmospheres and oceans*, *37*(4), 313–351.

Longuet-Higgins, M. S. (1953). Mass transport in water waves. *Philosophical Transactions of the Royal Society of London. Series A, Mathematical and Physical Sciences*, *245*(903), 535–581.

Madsen, O. S. (1978). Mass transport in deep-water waves. *Journal of Physical Oceanography*, *8*(6), 1009–1015.

Martinez, E., Maamaatuaiahutapu, K., & Taillandier, V. (2009). Floating marine debris surface drift: Convergence and accumulation toward the South Pacific subtropical gyre. *Marine Pollution Bulletin*, *58*(9), 1347–1355.

Maximenko, N., Hafner, J., & Niiler, P. (2012). Pathways of marine debris derived from trajectories of Lagrangian drifters. *Marine pollution bulletin*, *65*(1-3), 51–62.

McWilliams, J. C., & Restrepo, J. M. (1999). The wave-driven ocean circulation. *Journal of Physical Oceanography*, *29*(10), 2523–2540. https://doi.org/10.1175/1520-0485(1999)029<2523:TWDOC>2.0.CO;2

Mellor, G., & Blumberg, A. (2004). Wave breaking and ocean surface layer thermal response. *Journal of Physical Oceanography*, *34*(3), 693–698.

Mellor, G., & Yamada, T. (1982). Development of a turbulence closure model for geophysical fluid problems. *Reviews of Geophysics*, *20*(4), 851–875.

Onink, V., Wichmann, D., Delandmeter, P., & van Sebille, E. (2019). The role of Ekman currents, geostrophy, and Stokes drift in the accumulation of floating microplastic. *Journal of Geophysical Research: Oceans*, *124*(3), 1474–1490.

Polton, J. A., Lewis, D. M., & Belcher, S. E. (2005). The role of wave-induced Coriolis-Stokes forcing on the wind-driven mixed layer. *Journal of Physical Oceanography*, *35*(4), 444–457.

Rascle, N., & Ardhuin, F. (2013). A global wave parameter database for geophysical applications. part 2: Model validation with improved source term parameterization. *Ocean Modelling*, *70*, 174–188.

Rio, M.-H., Mulet, S., & Picot, N. (2014). Beyond GOCE for the ocean circulation estimate: Synergetic use of altimetry, gravimetry, and in situ data provides new insight into geostrophic and Ekman currents. *Geophysical Research Letters*, *41*(24), 8918–8925.

Saha, S., Moorthi, S., Pan, H.-L., Wu, X., Wang, J., Nadiga, S., et al. (2010). *NCEP climate forecast system reanalysis (cfsr) 6-hourly products, January 1979 to December 2010*. Research Data Archive at the National Center for Atmospheric Research, Computational and Information Systems Laboratory.

Sebille, E., Griffies, S., Abernathey, R., Adams, T., Berloff, P., Biastoch, A., et al. (2018). Lagrangian ocean analysis: Fundamentals and practices. *Ocean Modelling*, *121*, 49–75.

Seshasayanan, K., & Gallet, B. (2019). Surface gravity waves propagating in a rotating frame: The Ekman-Stokes instability. *Physical Review Fluids*.

Stanev, E. V., & Ricker, M. (2019). The fate of marine litter in semi-enclosed seas. Case of the Black Sea. *Frontiers in Marine Science*, *6*, 660.

Sterl, M. F., Delandmeter, P., & van Sebille, E. (2020). Influence of barotropic tidal currents on transport and accumulation of floating microplastics in the global open ocean. *Journal of Geophysical Research: Oceans*, *125*(2), e2019JC015583.

Suzuki, N., & Fox-Kemper, B. (2016). Understanding Stokes forces in the wave-averaged equations. *Journal of Geophysical Research: Oceans*, *121*(5), 3579–3596. https://doi.org/10.1002/2015JC011566

Terray, E., Drennan, W., & Donelan, M. (1999). *The vertical structure of shear and dissipation in the ocean surface layer*.

Tolman, H. L. (2009). User manual and system documentation of wavewatch III TM version 3.14. *Technical Note. MMAB Contribution*, *276*, 220.

Ursell (1950). On the theoretical form of ocean swell. On a rotating earth. *Geophysical Journal International*, *6*, 1–8.

van Sebille, E., Aliani, S., Law, K. L., Maximenko, N., Alsina, J., Bagaev, A., et al. (2020). The physical oceanography of the transport of floating marine debris. *Environmental Research Letters*, *15*(2), 023003.

van Sebille, E., Wilcox, C., Lebreton, L., Maximenko, N., Hardesty, B. D., van Franeker, J. A., et al. (2015). A global inventory of small floating plastic debris. *Environmental Research Letters*, *10*(12), 124006.

Xu, Z., & Bowen, A. (1994). Wave-and wind-driven flow in water of finite depth. *Journal of Physical Oceanography*, *24*(9), 1850–1866.

Zhang, H.-M., Reynolds, R., & Bates, J. (2006). *Blended and gridded high resolution global sea surface wind speed and climatology from multiple satellites: 1987-present*.